Effect of coastal boundary representation on basin-scale internal waves

Ito, Wataru

Nakayama, Keisuke

Shintani, Tetsuya

Effect of coastal boundary representation on basin-scale internal waves

Wataru Ito[a], Keisuke Nakayama[b]* and Tetsuya Shintani[c]

[a] *Graduate student, Graduate School of Engineering, Kobe University, Kobe, Japan*

Email: kyotamba1209@gmail.com

[b]*Professor, Graduate School of Engineering, Kobe University, Kobe, Japan*

Email: nakayama@phoenix.kobe-u.ac.jp (author for correspondence)

[c]*Associate Professor, Graduate School of Engineering, Tokyo Metropolitan University, Tokyo, Japan*

Email: shintani@tmu.ac.jp

Effect of coastal boundary representation on basin-scale internal waves

It is crucial to accurately reproduce internal Kelvin and Poincare waves under Coriolis forcing in numerical simulations for large-scale coastal environments. Therefore, for surface waves, the effects of horizontal grid representation on Kelvin and Poincare waves have been investigated using both structured and unstructured grid models. However, the effect of the grid representation on internal waves is poorly understood so far, especially for structured grids which uses a step-like lateral boundary. This study thus investigates the applicability of structured grids into internal Kelvin and Poincare waves using a circular basin to exclude the effect of open boundaries and discusses numerical errors in terms of the Rosbby-grid factor. Several different grid sizes were used for a structured grid simulation, which demonstrated that the structured grid simulation reproduced internal Kelvin and Poincare waves enough accurate compared to those obtained by the unstructured grid simulation. Furthermore, the structured grid simulation was also confirmed to agreed very well with the unstructured grid simulation in a conical basin which exhibits more realistic geometry. It was thereby shown the possibility that internal waves can be accurately analyzed using structured grids when the Rossby-grid factor is more than 10.

Keywords: Kelvin wave; Poincare wave; structured grid; unstructured grid; Rossby-grid factor

1 Introduction

In a stratified fluid, such as coastal areas, the ocean and lakes, internal waves play a significant role in not only mass transport and energy transfer but also vertical mixing (Gloor et al., 1994; Pierson and Weyhenmeyer, 1994; Steinman et al., 1997; Wüest and Lorke, 2003; Helfrich and Melville, 2006; Nakayama et al., 2012; Lin et al., 2021). Additionally, when strong wind blows over a fjord coast, bottom water masses can come into surface layers due to upwelling, which may affect fisheries and ecological systems (Asplin et al., 1999). Also, the same phenomena are revealed to occur in a stratified lake (Finlay et al. 2001). Upwelling is associated with enclosed bay-scale (basin-scale) internal waves, and Thompson & Imberger (1980) and Imberger & Hamblin (1982) applied the Wedderburn number to estimate the criteria for the occurrence of upwelling without a rotation effect, i.e., the Coriolis effect in a

rectangular basin (Stevens and Imberger, 1996). The sloping bottom geometry and generic horizontal basin shape are separately quantified in terms of suitable generalizations of the Wedderburn number (Shintani et al., 2010). However, the generalized Wedderburn numbers cannot be applied to an enclosed bay where the scale is larger than the internal radius of deformation (Rossby radius). In previous studies, since the Coriolis effect was found to cause locally-intense mass transport, such as an anti-cyclonic boundary current that is the scale of the Rossby radius (Wake et al., 2004; Wake et al., 2005; Ulloa et al., 2014), it is necessary to clarify the relationship between basin-scale internal waves and Coriolis forcing (Csanady, 1972a and 1972b; Antenucci and Imberger, 2001; Ulloa et al., 2015; Rojas et al., 2018; Nakayama et al., 2020b).

In a stratified fluid subject to Coriolis forcing there are many difficulties in analyzing internal waves theoretically, so numerical simulations have been applied to analyze internal Kelvin waves (IKWs), internal Poincare waves (IPWs) and the other high-frequency internal waves (Hodges et al., 2000; Laval et al., 2003; Rueda et al., 2003). In the case of internal wave breaking over a slope in coastal areas, accurate numerical simulations have successfully evaluated the breaking process and energy dissipation using structured grids (Vlasenko and Hutter, 2002; Aghsaee et al., 2010; Arthur and Fringer, 2014; Nakayama et al., 2019). However, Hodges et al. (2000) suggested that it is necessary to verify the validity of structured grid representation for the computational domain with curve-lined horizontal boundaries to analyze the basin-scale internal waves in a stratified fluid. In contrast to a structured grid system, there are several methods to fit a grid to curved boundaries using unstructured grids, such as a triangle-shaped polygon to overcome this problem (Casulli and Walters, 2000; Chen et al., 2003; Fringer et al., 2006; Zhang and Baptista, 2008; Steinmoeller et al., 2019). In general, structured grid models have significant advantages in pre-processing, such as grid generation and post-processing, including extraction of point and cross-section data. The Cartesian (or matrix) data structure fits well with our way of thinking. Consequently, most geophysical data, such as bathymetry data, are provided in a structured format. Although there is excellent software for unstructured grid generators such as GMSH and interpolating data on an unstructured grid such as Matlab, we usually prefer simplistic and straightforward software. Therefore, a structured grid system would be a preferable choice if computed results are obtained with acceptable accuracy.

In the case when the amplitude of surface and internal waves is small enough, theoretical solutions exist for IKWs and IPWs in a circular basin with Coriolis forcing (Csanady, 1967; Birchifield, 1969; Antenucci et al., 2001; Stocker et al., 2003). For surface waves, an unstructured grid system was applied to surface Kelvin waves (SKWs) and surface Poincare waves (SPWs) to successfully reproduce the theoretical solutions proposed by Csanady (1967) and Birchfield (1969) (Chen et al., 2007; Walters et al., 2009). In contrast to surface waves, regardless of the grid system, there are few numerical studies comparing with the theoretical solutions for internal waves because the pycnocline needs to have a finite thickness in three-dimensional level models, but the thickness is assumed to be zero in theory. Interestingly, in many previous studies related to basin-scale internal waves, structured grids were applied, and good agreements were obtained between numerical and observed results (Laval et al., 2003; Hodges et al., 2010). Schwab & Beletsky (1998) demonstrated that the grid size should be less than one-fifth of the Rossby radius in a coastal area (Beletsky et al., 1997). However, the limitations and criteria for boundary representation for IKWs and IPWs are not well discussed so far.

This study thus aims to investigate how accurately structured grids can be applied to basin-scale surface and internal waves in a circular basin compared to unstructured grids and theoretical solutions. The theoretical solutions by Csanady (1967) and Birchifield (1969) were used both for surface and internal waves, and a three-dimensional environmental model, Fantom, was employed to obtain numerical results for structured and unstructured grids (Nakayama et al., 2012; Nakayama et al., 2014; Nakayama et al., 2020a). For structured grids, three different grid sizes were tested for surface waves and four grid sizes for internal waves to clarify the effect of grid size on the computational accuracy. Firstly, the surface wave problem was discussed with the theoretical solutions same as the previous researches. Then, for internal waves, to compare the numerical results with theoretical ones for flat-circular basin, we derived a modified theoretical solution taking account of attenuation effects due to viscosity and thick pycnocline in 3D numerical models. Lastly, the validity of structured grids for IKWs and IPWs in a three-dimensional stratified fluid was investigated in terms of Rossby-grid factor using a more general bottom topography, conical basin.

2 Methods

2.1 theoretical solutions

Normalized longwave equations in a circular basin are obtained by assuming that the amplitude of waves is small compared to the representative water depth and by neglecting the higher-order terms as follows (Csanady, 1967; Birchifield, 1969; Antenucci et al., 2001; Stocker et al., 2003):

$$\frac{\partial u}{\partial \tau} - v = -\frac{\partial \eta}{\partial r} \tag{1}$$

$$\frac{\partial v}{\partial \tau} + u = -\frac{\partial \eta}{r\partial \theta} \tag{2}$$

$$\frac{u}{r} + \frac{\partial u}{\partial r} + \frac{\partial v}{r\partial \theta} = -\frac{\partial \eta}{\partial \tau} \tag{3}$$

$$r' = R_0 r \tag{4}$$

$$R_0 = \frac{c_w}{f_C} \tag{5}$$

$$u' = c_w u \tag{6}$$

$$v' = c_w v \tag{7}$$

$$\tau = f_C t' \tag{8}$$

$$\eta' = H\eta \tag{9}$$

where (u', v') is the velocity in the horizontal plane, (r', θ) is the polar coordinate, R_0 is the Rossby radius, t' is the time, η' is the water surface or density interface elevation, H is the representative water depth, c_w is the wave speed, g is the gravity acceleration, f_C is the Coriolis parameter, and the variables without the apostrophe symbol are the normalized variables.

For surface waves, H is the total water depth and c_w is the linear surface longwave speed ($= \sqrt{gH}$) in Equations (1) to (3). For internal waves, H is the water

depth of the lower layer and c_w is the linear internal longwave speed ($= \sqrt{(\rho_2 - \rho_1)gh_1h_2/\{\rho_2(h_1 + h_2)\}}$) in Equations (1) to (3) when the water depths of the upper and lower layers are h_1 and h_2 and the densities of the upper and lower layers are ρ_1 and ρ_2 in a two-layer fluid. Normalized dispersion relationships for each mode were obtained as Equation (10) from the Bessel equation.

$$1 - \sigma_k M^2 = 0 \tag{10}$$

$$\mathrm{M} = \frac{z_k I_0(z_k)}{I_1(z_k)} - 1 \tag{11}$$

$$\mathrm{z_k} = S^{-1}\sqrt{1 - \sigma_k^2} \tag{12}$$

$$S = \frac{c}{f_C r_0} \tag{13}$$

where k is the mode number, σ_k is the normalized frequency, S is the Burger number, I_0 is the modified Bessel function of the first kind of 0th order, and I_1 is the 1st order.

By giving normalized frequency, σ_k, the surface or interface displacement for each mode k, η_k, and the total displacement of surface or interface, η, are obtained as follows:

$$\eta_\mathrm{k}(\mathrm{r}, \theta, \tau) = \frac{1}{2} G_k(r)\cos(n\theta - \sigma_k \tau) \tag{14}$$

$$\eta(\mathrm{r}, \theta, \tau) = \sum_{k=1}^{\infty} \frac{1}{2} G_k(r)\cos(n\theta - \sigma_k \tau) \tag{15}$$

$$\mathrm{G_k}(r) = \begin{cases} J_n\left(\dfrac{f_C r\sqrt{\sigma_k^2 - 1}}{c}\right) & |\sigma_k| > 1 \\ I_n\left(\dfrac{f_C r\sqrt{\sigma_k^2 - 1}}{c}\right) & |\sigma_k| < 1 \end{cases} \tag{16}$$

where η_k is the water surface or density interface elevation for mode k, and η is the water surface or density interface elevation.

To include the effect of wind stress which is given uniformly and continuously over a circular basin, Equations (1) & (2) are deformed into Equations (17) & (18) by adding the external forces (Stocker et al., 2003).

$$\frac{\partial \mathrm{u}}{\partial \tau} - v = -\frac{\partial \eta}{\partial \mathrm{r}} + SW_F^{-1}cos\theta \tag{17}$$

$$\frac{\partial v}{\partial \tau} + u = -\frac{\partial \eta}{r\partial \theta} - SW_F^{-1}sin\theta \tag{18}$$

$$W_F = \frac{gH^2}{Fr_0} \tag{19}$$

$$F(\tau) = \begin{matrix} 0, & \tau < 0 \\ F, & \tau \geq 0 \end{matrix} \tag{20}$$

$$F = \frac{1}{H}\frac{\rho_{air}}{\rho_w}\frac{C_D}{2}|U_w|U_w \tag{21}$$

where ρ_{air} is the atmospheric density, ρ_w is the water density, C_D is the bulk friction coefficient for wind force, and U_w is the wind speed.

Finally, the theoretical solutions under wind stress are given as follows:

$$\eta(\mathrm{r},\theta,\tau) = (W_C^{-1}Q_C - W_F^{-1}Q_F)cos\theta - (\mathrm{W_C^{-1}} - \mathrm{W_F^{-1}})\sum \mathrm{a_k}D_kA_k \tag{22}$$

$$\mathrm{W_C} = HC^{-1}r^{-1} \tag{23}$$

$$\mathrm{Q_C} = rS - A_0 \tag{24}$$

$$\mathrm{Q_F} = -\mathrm{A_0} \tag{25}$$

$$\mathrm{a_k} = \frac{\sigma_k - 1}{1 + \sigma_k - S^{-2}\sigma_k^3} \tag{26}$$

$$\mathrm{D_k} = \cos(\theta - \sigma_k\tau) \tag{27}$$

$$\mathrm{A_k} = \frac{I_1(r'z_kS)}{I_1(z_k)} \tag{28}$$

where *C* is the initial linear gradient of water surface level.

169

170 ***2.2 Numerical computations***

171 A three-dimensional non-hydrostatic model, Fantom, was used to analyze wave
172 motions in a circular basin. Fantom is an object-oriented parallel computing model that
173 has been applied to investigate, not only real scale phenomena (Nakamoto et al., 2013;
174 Nakayama et al., 2014; Nakayama et al., 2016), but also laboratory-scale phenomena
175 (Nakayama et al., 2012; Nakayama et al., 2019; Nakayama et al., 2020b). Fantom uses
176 a turbulence closure based on the generic length-scale (GLS) equation model in a real
177 scale phenomenon (Jones and Launder, 1972; Umlauf & Burchard, 2003), together with
178 the partial cell scheme used to represent a sub-grid scale elevation of a sloping boundary
179 in the z-coordinate bathymetry (Adcroft, 1997). To investigate the effect of grid sizes
180 on computational accuracy, three different grid sizes for surface waves and four grid
181 sizes for internal waves were used in the numerical simulations for structured grid
182 simulations, in which the grid-size condition of 1000 m for internal waves is shown in
183 "Discussion" for more detailed analysis (Table 1). For time marching, the theta method
184 was applied for surface waves with $\theta = 0.5$ which results in second-order accuracy in
185 time. In contrast, the second-order Admas-Bashforth method is used for the advection
186 of scalars which represents the internal waves.

187 For surface waves, conditions of H = 75 m, r_0 = 67500 m and f_C = 10^{-4} s^{-1} were
188 given by following Birchifield (1969). The grid sizes for structured grids were 1000 m,
189 2500 m and 5000 m with the time steps of 5 s, 10 s and 15 s, respectively (Figure 1).
190 Since the wind stress is small and the surface displacement is also small, the
191 representative velocity for computing the Courant-Friedrichs-Lewy condition (CFL
192 condition) is a linear longwave speed (c_w = 27.1 m s^{-1}), which results in CFL
193 conditions of 0.14, 0.11 and 0.08 for grid sizes of 1000 m, 2500 m and 5000 m,
194 respectively. In the numerical simulation for unstructured grids, the representative grid
195 size was 1780 m with a time step of 15 s, which corresponds to a CFL condition of 0.23.
196 To investigate the relationship between the Rossby radius and the grid size on
197 computational accuracy, we define the Rossby radius / the grid size as "Rossby-grid
198 factor". Since the Rossby radius was 2.71 x10^5 m, the Rossby-grid factors were 270,
199 108 and 54 for the grid sizes of 1000 m, 2500 m and 5000 m in structured grid
200 simulations, respectively (Table 1).

For internal waves, conditions of h_1 = 15 m, h_2 = 15 m, ε = 0.00198 ($\varepsilon = (\rho_2 - \rho_1)/\rho_2$), r_0 = 10000 m and f_C = 8.37x10^{-5} s^{-1} were given by following Antenucci et al. (2001) and Stocker et al. (2003). Linear longwave speed for internal waves is c_w = 0.38 m s^{-1}, which corresponds to the Rossby radiuses of 20430 m and 4540 m, respectively. The grid sizes for structured grid simulations were 100 m, 200 m and 500 m, in which the corresponding time steps were 10 s, 20 s, and 30 s (Figure 2). The CFL conditions were 0.038, 0.038, and 0.022, and the Rossby-grid factors were 45, 23 and 9, respectively (Table 1). Therefore, the Rossby-grid factors were confirmed to be larger than 5, which was the recommended minimum value by Schwab & Beletsky (1998). For the unstructured grid simulation, the representative length scale and time step were 500 m and 20 s, which gives a CFL condition of 0.015. In a three-dimensional numerical simulation, the turbulence closure was needed to transfer the wind stress from the surface to deeper grid levels, which build up the surface displacement, and in turn lead to pycnocline displacement. A turbulent closer model, the GLS equation model using $k - \varepsilon$ model with the CA filter, was used (Umlauf & Burchard, 2003; Warner et al., 2005). The turbulent shear also occurs across the pycnocline and reduces the kinetic energy of the internal waves.

The Coriolis parameters for surface and internal waves were f_C = 10^{-4} s and f_C = 8.37x10^{-5} s^{-1}, and the representative time scales were $1/f_C$ = 2.8 h and $1/f_C$ = 3.3h, respectively. Boegman et al. (2005) revealed that total potential energy in a circular domain due to wind stress disappears due to dissipation by the breaking of high-frequency internal waves over sloping bottoms within a half of the period of mode 1 internal waves. In this study, peripheral lengths for surface and internal waves were 4.241 x10^5 m and 6.28 x10^4 m. As the linear longwave speeds are 27.1 m s^{-1} and 0.38 m s^{-1}, the periods of mode 1 longwave were 4.3 h and 45.9 h for surface and internal waves. Thus, potential energy due to wind stress is expected to disappear within at least about 20 h in both cases. Therefore, we define 20 h as an energy time scale (= T_E) in this study and investigate the validity of numerical simulation results within T_E. Note that the same energy time scale as internal waves was applied to surface waves because the time scale of surface waves is shorter than internal waves.

3 Results

3.1 Surface waves

Equation (10) gives normalized frequencies for surface waves of mode 1 to mode 8 with the conditions of H = 75 m, r_0 = 67500 m, and f_C = 10^{-4} s^{-1} (Table 2). Few studies show the value of the normalized frequency explicitly, and it was found that the normalized frequencies for mode 1 to mode 4 by Birchfield (1969) should be replaced by Table 2. A Mode 1 surface wave corresponds to SKW, which has the largest amplitude at the curve-lined boundary and propagates in the cyclonic direction because of the positive normalized frequency (Figure 3a). Surface waves more than or equal to mode 2 correspond to SPWs, which have characteristics of large amplitude around the centre of the circular basin (Figures 3b and 3c). While SPW of mode 2 has anti-cyclonic direction due to the negative normalized frequency, SPW of mode 3 has a cyclonic direction with the positive normalized frequency (Table 2). In Figure 3, the maximum amplitude is normalized to 1.0 to show the relative magnitude of each mode clearly.

Numerical simulations were carried out by following previous studies, which applied uniform and constant Northwind with a wind speed of 3.21079 m s^{-1} (Csanady, 1967; Birchifield, 1969; Stocker et al., 2003). The displacements of surface waves at $(x,\ y)$ = (67500 m, 101250 m) as shown in Figure 1 were examined. The characteristics of SKW and SPW appear clearly in this location (Figure 4). It was demonstrated that the displacements of surface waves with the different grid sizes do not change a lot until T_E = 20 h even if the grid size changes from 1000 m to 5000 m (Figure 4a). To evaluate the accuracy of numerical simulations, we define $Er = \int_0^{T_E} |\eta - \eta_T| dt / \int_0^{T_E} \eta_T dt$ (η is the surface displacement at the target location and η_T is a benchmark displacement). Here, the theoretical surface displacement is used as the benchmark. We obtained Er of 2.1 %, 6.5 % and 8.5 % for grid sizes of 1000 m, 2500 m and 5000 m, respectively (Table 1). It was thus confirmed that the numerical simulation with the structure grids has enough accuracy in estimating the displacement of surface waves even in the largest grid size, 5000 m. On the other hand, unstructured grid computation showed excellent agreement with the theoretical solutions with Er = 0.7 %, though the representative scale is 1780 m. Therefore, unstructured grid simulation was found to provide more accurate computational results than those obtained by the structured grids, as had been expected.

3.2 Internal waves

The normalized frequency for internal waves was obtained using Equation (10) with conditions of h_1 = 15 m, h_2 = 15 m, ε = 0.00198, r_0 = 10000 m and f_C = 8.37x10^{-5} s^{-1} (Table 3). The normalized frequency of mode 1 to mode 8 is shown though Stocker & Imberger (2003) showed the normalized frequency only up to mode 2. The characteristic of each mode is the same as the surface waves (Figure 3). In a three-dimensional numerical simulation using a level model, it is necessary to use a vertically fine grid size around the pycnocline to reduce numerical errors. Therefore, in this study, the vertical grid sizes were set as 0.5 m x 26, 0.25 m x 4, 0.1 m x 20, 0.25 m x 4 and 0.5 m x 33 layers from the flat bottom boundary to the surface, so that the total number of vertical grids was 87 and a minimum grid size of 0.1m was used around the pycnocline. The vertical profile of density was given by using a function of $\tanh(\alpha_I z)$ with α_I = 0.5 m. Numerical simulations were carried out by applying uniform and constant North winds with a wind speed of 2.0 m s^{-1}.

In a two-layer system, it is possible to ignore the effect of the shear between the upper and lower layers because the thickness of the pycnocline is zero, and there is no transfer of the momentum. To include the effect of shear, it is necessary to add a friction term. On the other hand, in a three-dimensional numerical simulation, a pycnocline has a finite thickness which fundamentally includes the shear advection term in the momentum equations, which results in the attenuation of the amplitude of density interface displacement and a decrease in the internal wave speed. To include their effects on the theoretical solutions, the attenuation rate of the amplitude and the decreasing factor in the internal wave speed were added as Equation (29). Since it was found from the surface wave analysis that unstructured grid simulation can provide high applicability, we decided to use an unstructured grid simulation to obtain the parameters of Equation (29). The best-fit curves were given using an attenuation rate of the amplitude, $e^{-3.0\times10^{-7}t}$, and a decreasing factor in the internal wave speed, 93 % of a linear longwave speed, at (x, y) = (10000 m, 15000 m) as shown in Figure 2 (Figure 5a). Although the theoretical solution is similar to the unstructured grid simulations, it was difficult to fit the theoretical result to the numerical results completely, i.e., we cannot use the theoretical solution as a benchmark for internal wave analysis.

$$\mathrm{H}(\mathrm{r},\theta,\tau) = e^{-3.0\times10^{-7}t}\sum_{k=1}^{\infty}(W_C^{-1}Q_C - W_F^{-1}Q_F)cos\theta \\ -\left(\mathrm{W_C^{-1}} - \mathrm{W_F^{-1}}\right)\sum \mathrm{a_k} D_k A_k \tag{29}$$

So, in this study, the effect of grid size in the structured grid computations was investigated by comparing with the unstructured grid simulation as a reference (Figure 5b). Er was obtained for internal waves as the same with the surface waves, 7.5 %, 11.0 % and 12.8 % for grid sizes of 100 m, 200 m and 500 m, respectively (Table 1). Since the lateral boundary is reproduced using a step-like function in a structured grid simulation, strong shear damping due to local acceleration (numerical error in advection term) is expected to occur around the domain boundaries, which may result in larger Er for internal waves compared to the surface wave analysis. However, Er is still small enough to analyze the density interface displacement. Interestingly, Er does not vary a lot with the change in grid size, which suggests that the energy loss due to the step-like boundary does not change greatly with the grid size by up to the Rossby-grid factor of 9 in Table 1. Therefore, it was found that a structured grid simulation can provide sufficiently high accuracy for internal wave analysis even though the grid size becomes larger, up to about 2.5 % compared to the computational domain scale.

4 Discussion

To understand how accurately a structured-grid simulation reproduces basin-scale waves, the surface and density interface displacements at the energy time scale, T_E, were compared to the theoretical solution and the unstructured grid simulation (Figures 6 and 7). For surface waves, it was confirmed that SKWs and SPWs exist in the theoretical solution and unstructured grid simulation (Figures 6a and 6b). The structured grid simulation with 1000 m grids was shown to agree with the unstructured grid simulation as well. However, SPWs around the centre of the circular basin had slightly smaller amplitude in structured grid simulations with 2500 m and 5000 m grids compared to the unstructured grid simulation.

For internal waves, it is apparent that IKWs dominate because the Rossby radius is 4540 m, which is much smaller than the 20000 m diameter of the circular basin (Figure 7). Therefore, the effect of IPWs on the amplitude could be seen slightly around the

centre of a circular basin. All structured grid simulations show good agreement with the unstructured grid simulation (Figures 7b to 7e).

Since Er did not vary very much with the change in the grid size in Figure 5, it may also suggest the possibility that a structured grid simulation can provide sufficiently good and practical computational results for internal wave analysis within the energy time scale, T_E. Schwab & Beletsky (1998) suggested applying the grid size less than one-fifth of the Rossby radius in coastal regions though our study recommends applying the Rossby-grid factor of 9. To clarify the effect of the grid size on internal waves, we conducted an additional numerical simulation with the grid size of 1000 m (the Rossby-grid factor is 5), which shows that Er is 16.6 % (Table 1). Since Er increases rapidly from the Rossby-grid factor of 9 to 5 ((12.8 % - 11.0 %)/(9 – 5) = 0.95) compared to the Rossby-grid factor of 23 to 9 ((16.6 % - 12.8 %)/(23 – 9) = 0.13), it may be suggested that the Rossby-grid factor should be more than 9, approximately, the Rossby-grid factor of 10.

The previous studies demonstrated that reflection of internal waves by obstacles can be estimated theoretically when internal waves propagate over a step-like topography representing a Gaussian bump at the bottom (Simanjuntak et al., 2009). The theoretical solutions are based on a weakly nonlinear theory, and reliable to the varying bottom topography, heightening less than 10 % of the total water depth. Still, it could be possible to apply a similar strategy into our study to clarify the characteristics of grid size effect on the generation of internal waves in a circular basin. Simanjuntak et al. (2009) found that the generation of high-frequency internal waves due to step-like grids is explained using the topography's Fourier transform. Thus, high-frequency internal waves are expected to occur at adjacent frequencies of f_G in the structured grid system due to the step-like lateral boundary as follows (Simanjuntank et al., 2009):

$$f_G = \frac{1}{4\Delta L} \tag{30}$$

where f_G is the significant and dominant frequency due to the step-like lateral boundary of the structured grid system, and ΔL is the grid size.

The spectrum of time series of the density interface displacement was calculated at (x, y) = (10000 m, 15000 m) for the unstructured, 500 m and 1000 m grid simulations to investigate the criteria of the Rossby-grid factor between 5 and 10 (Figure 8). The unstructured grid simulation was again considered as a benchmark result. The 500 m and 1000 m grid simulations correspond to the Rossby-grid factor of 10 and 5. In Figure

8, temporal frequency is converted into spatial frequency using an internal long-wave speed of 0.38 m s^{-1}. As shown in the theoretical solutions, dominant modes 1 & 2 have larger amplitude than the other modes (Table 3). The amplitudes of the dominant modes in the 500 m grids were almost the same as the unstructured grid, but the 1000 m grids' amplitudes were smaller than the unstructured grid. The peak amplitudes at high frequencies more than f_G did not occur in the structured grids although high-frequency peak amplitudes existed in the unstructured grids. Thus, higher frequency internal waves might be suppressed due to the step-like lateral boundary. Significantly, f_G of the 1000 m grids was almost the same as $1/R_0$, which corresponds to the Rossby-grid factor of 4.5, and the peak amplitude around $1/R_0$ did not appear in the 1000 m grids but in the other grids shown by green circles in Figures 8(a) and 8(b). It is conjectured that the energy reduction of the dominant modes 1 & 2 may be caused by the interaction between the near-inertial internal wave and the high-frequency internal waves of f_G in the 1000m grids. Therefore, we may again suggest that the ideal Rossby-grid factor should be more than 10 for the structure grids.

An unstructured grid system can provide fine grids to reproduce accurate lateral boundaries. On the other hand, there are some techniques for a structured grid system to provide fine local grids, such as nesting grid and tree-based grid techniques. With these techniques, we can improve the boundary representation of a structured grid model. Therefore, we additionally examine the effectiveness of local mesh refinement on IKWs and IPWs. We gave 100 m grids along the lateral boundaries to smoothen the lateral edges and 200 m & 400 m grids elsewhere (Figure 9a) while keeping external force conditions similar to the previous internal wave case. There was a slight difference between the locally refined grid and 100 m uniform grid, i.e., the former showed slightly higher displacements of the density interface at crests than 100 m uniform grids (Figure 9b). However, the time series of density interface level was almost the same as the 100 m grid simulation. Thus, the local mesh refinement would be practical and effective to represent lateral boundaries in a stratified fluid.

Since water depth varies in actual coastal areas, it is conceivable that internal waves are affected by the topography and that the energy dissipates more than in a circular basin. Therefore, we attempted to investigate how internal waves behave in a conical basin that is more realistic than a circular one (Figure 10a). The maximum water depth was 30 m at the centre of the basin, and the upper- and lower-layer depths were the

same, 15 m. Two different numerical simulations were carried out using structured and unstructured grids. In the unstructured grid simulation, the representative grid size was 500 m (Table 1). As there was no considerable difference in Er among the three different structured grids in the internal wave analysis of a circular basin, the same grid size chaof 500 m was used in the structured grid simulation. Although, in the analysis of the circular basin, constant and uniform winds were given to compare to the theoretical solution, it is unusual to apply steady and consistent wind speed for 20 h in a real situation. Therefore, we carried out numerical simulations starting from tilting density interface with a gradient of 1/20000 without external forces (Figure 10a).

Density interface displacements were compared at (x, y) = (10000 m, 12500 m) where IKW and IPW may play a significant role in the interface displacement (Figure 10). The peripheral length for internal waves is half as much as a circular basin, which corresponds to an energy time scale, T_E, of 10 h. However, we applied T_E = 20 h instead of T_E = 10 h to compare with the numerical simulations in the circular basin. There was no considerable difference between the unstructured and structured grid simulations, and the difference, Er, was obtained as 5.7 % (Figure 10b). Although energy dissipation due to friction at the bottom was not included in numerical simulations, we conjecture that kinetic energy decreased due to the occurrence of large velocities in the lower layer around the shallow lateral boundaries. The decrease in energy is apparent from the horizontal distribution of density interface displacement, which showed a noticeable decline in the amplitude at the lateral boundaries at 10 h and 20 h compared to the initial condition (Figure 11). In actual coastal areas, energy dissipation occurs due to the deformation of low-frequency internal waves to high-frequency internal waves and the breaking of internal solitary waves over a sloping bottom. Therefore, IKW and IPW would lose their energy more in actual coastal areas than in our analysis, which may suggest the possibility that a structured grid simulation can reproduce flow field in a stratified fluid sufficiently for scientific and engineering purposes.

A structured grid simulation has almost the same accuracy as an unstructured grid simulation when the Rossby-grid factor is more than approximately 10. With this criterion, we can positively and confidently employ a structured grid model to investigate the basin-scale internal waves. This paper does not intensify the structured grid's benefits; instead, we try to remove uncertainties using the structured grid model

for basin-scale internal waves. Additionally, it is not reliable to compare the speed performance between models as it largely depends on several factors such as schemes, solvers and implementations. Therefore, we cannot specify the computational evaluation between the structured and unstructured grid systems.

5 Conclusions

The Rossby radius / the grid size was defined as "Rossby-grid factor" to discuss the effect of grid size on basin scale waves. For surface waves, the unstructured grid simulation was found to agree with the theoretical solution very well, with Er = 0.7 % with the Rossby-grid factor of 152. The structured grid simulations showed practically small errors with the Rossby-grid factors of 270, 108 and 54. Even in the large grid simulation, accurate numerical simulation results were obtained.

For internal waves, it was shown that the proposed theoretical solution could not agree with the actual internal wave displacements because the pycnocline has a finite thickness in a three-dimensional numerical simulation while the theory assumes a zero thickness pycnocline and the effect of turbulence on internal waves is omitted. Since an unstructured grid simulation was revealed to reproduce SKWs and SPWs perfectly, we employed an unstructured grid simulation as a benchmark for internal wave analysis. Er was obtained as 7.5 %, 11.0 %, 12.8 % and 16.6 % for grid sizes of 100 m, 200 m, 500 m and 1000 m with the Rossby-grid factors of 45, 23, 9 and 5, respectively. Although Er was larger than surface waves due to the occurrence of numerical dissipation by step-like grids at the lateral boundaries, reasonably good simulation results were obtained with the Rossby-grid factor more than 9. Additionally, to clarify the applicability of structured grids into a real scale, numerical simulations were carried out using a conical basin. The same grid size was used for the structured and unstructured grid simulations, and we applied the unstructured grid simulation as a benchmark with the Rossby-grid factor of 23, which resulted in Er = 5.7 % that was smaller than a circular basin. Therefore, it was concluded that IKWs and IPWs could be reproduced sufficiently well using structured grids when the Rossby-grid factor is more than approximately 10.

Acknowledgements

This work was supported by the Japan Society for the Promotion of Science under grant 18H01545 and 18KK0119.

References

Reference

1) Adcroft, A. J., C. N. Hill, and J. Marshall. 1997. “Representation of topography by shaved cells in a height coordinate ocean model.” *Monthly Weather Review* 125: 2293-2315.
2) Aghsaee, P., L. Boegman, and K. G. Lamb. 2010. “Breaking of shoaling internal solitary waves.” *Journal Fluid Mechanics* 659: 289-317.
3) Antenucci, J. P., and J. Imberger. 2001. “Energetics of long internal gravity waves in large lakes.” *Limnology and Oceanography* 46: 1760-1773.
4) Arthur, R. S., and O. B. Fringer. 2014. “The dynamics of breaking internal solitary waves on slopes.” *Journal Fluid Mechanics* 761: 360-398.
5) Asplin, L., A. G. V. Salvanes, and J. B. Kristoffersen. 1999. “Nonlocal wind-driven fjord-coast advection and its potential effect on plankton and fish recruitment.” *Fisheries Oceanography* 8: 255-263.
6) Beletsky, D., W. P. O’Connor, D. J. Schwab, and D. E. Dietrich. 1997. “Numerical simulation of internal Kelvin waves and coastal upwelling fronts.” *Journal of Physical Oceanography* 27: 1197-1215.
7) Birchfield, G. E. 1969. “Response of a circular model Great Lake to a suddenly imposed wind stress.” *Journal of Geophysical Research* 74: 5547-5554.
8) Boegman, L., G. N. Ivey, and J. Imberger. 2005. “The degeneration of internal waves in lakes with sloping topography.” *Limnology and Oceanography* 50(5): 1620-1637.
9) Casulli, V., and R. A. Walters. 2000. “An unstructured grid, three-dimensional model based on the shallow water equations.” *International Journal for Numerical Methods in Fluids* 32: 331-348.
10) Chen, C. S., H. S. Huang, R. C. Beardsley, H. D. Liu, Q. C. Xu, and G. Cowles. 2007. “A finite-volume numerical approach for coastal ocean circulation studies: comparisons with finite difference models.” *Journal of Geophysical Research* 112, C03018. doi:10.1029/2006JC003485.
11) Chen, C., H. Liu, and R. C. Beardsley. 2003. “An unstructured grid, finite-volume, three- dimensional, primitive equations ocean model: applications to coastal ocean and estuaries.” *Journal of Atmospheric and Oceanic Technology* 20: 159-186.
12) Csanady, G. T. 1967. “Large-scale motion in the great lakes.” *Journal of*

Geophysical Research 72(16): 4151-4162.

13) Csanady, G. T. 1972a. “The coastal boundary layer in Lake Ontario: Part II. The summer-fall regime.” *Journal of Physical Oceanography* 2: 168-176.

14) Csanady, G. T. 1972b. “The coastal boundary layer in Lake Ontario. Part I: The Spring Regime.” *Journal of Physical Oceanography* 2: 41-53.

15) Finlay, K. P., H. Cyr, and B. J. Shuter. 2001. “Spatial and temporal variability in water temperatures in the littoral zone of a multibasin lake.” *Canadian Journal of Fisheries and Aquatic Sciences* 58: 609-619. doi:10.1139/cjfas-58-3-609.

16) Fringer, O. B., M. Gerritsen, and R. L. Street. 2006. “An unstructured-grid, finite-volume, nonhydrostatic, parallel coastal ocean simulator.” *Ocean Modelling* 14: 139-173.

17) Gloor, M., A. Wüest, and M. Münnich. 1994. “Benthic boundary mixing and resuspension induced by internal seiches.” *Hydrobiologia* 284: 59-68. doi:10.1007/BF00005731.

18) Helfrich, K. R., and W. K. Melville. 2006. “Long nonlinear internal waves.” *Annual Review of Fluid Mechanics* 38: 395-425.

19) Hodges, B. R., J. Imberger, A. Saggio, and K. B. Winters. 2010. “Modeling basin-scale internal waves in a stratified lake.” *Limnology and Oceanography* 45: 1603-1620.

20) Imberger, J., and P. F. Hamblin. 1982. “Dynamics of lakes, reservoirs and cooling ponds.” *Annual Review of Fluid Mechanics* 14: 153-187. doi:10.1146/annurev.fl.14.010182.001101.

21) Jones, W. P., and B. E. Launder. 1972. “The prediction of laminarization with a two-equation model of turbulence.” *International Journal of Heat and Mass Transfer* 15: 301-314.

22) Laval, B. E., J. Imberger, B. R. Hodges, and R. Stocker. 2003. “Modeling Circulation in Lakes: Spatial and Temporal Variations.” *Limnology and Oceanography* 48: 983-994. doi:10.4319/lo.2003.48.3.0983.

23) Lin, H. C., C. Y. Chiu, J. W. Tsai, W. C. Liu, K. Tada, and K. Nakayama. 2021. “Influence of thermal stratification on seasonal net ecosystem production and dissolved inorganic carbon in a shallow subtropical lake.” *Journal of Geophysical Research* online. https://doi.org/10.1029/2020JG005907.

24) Nakamoto, A., K. Nakayama, T. Shintani, Y. Maruya, K. Komai, T. Ishida, and Y. Makiguchi. 2013. “Adaptive management in Kushiro Wetland in the context of salt

526 wedge intrusion due to sea level rise." *Hydrological Research Letters* 7(1): 1-5.
527 25) Nakayama, K., H. D. Nguyen, T. Shintani, and K. Komai. 2016. "Reversal of
528 secondary circulations in a sharp channel bend." *Coastal Engineering Journal* 58,
529 1650002.
530 26) Nakayama, K., T. Sato, K. Shimizu, and L. Boegman. 2019. "Classification of
531 internal solitary wave breaking over a slope." *Physical Review Fluids* 4, 014801.
532 27) Nakayama, K., T. Sato, K. Tani, L. Boegman, I. Fujita, and T. Shintani. 2020b.
533 "Breaking of internal Kelvin wave shoaling on a slope." *Journal of Geophysical*
534 *Research* 125. Advance online publication.
535 28) Nakayama, K., T. Shintani, K. Kokubo, T. Kakinuma, Y. Maruya, K. Komai, and
536 T. Okada. 2012. "Residual current over a uniform slope due to breaking of internal
537 waves in a two-layer system." *Journal of Geophysical Research* 117, C10002.
538 doi:10.1029/2012JC008155.
539 29) Nakayama, K., T. Shintani, K. Komai, Y. Nakagawa, J. W. Tsai, D. Sasaki, K. Tada,
540 H. Moki, T. Kuwae, K. Watanabe, and M. R. Hipsey. 2020a. "Integration of
541 Submerged Aquatic Vegetation Motion Within Hydrodynamic Models." *Water*
542 *Resources Research* 56, 027369.
543 30) Nakayama, K., T. Shintani, K. Shimizu, T. Okada, H. Hinata, and K. Komai. 2014.
544 "Horizontal and residual circulations driven by wind stress curl in Tokyo Bay."
545 *Journal of Geophysical Research* 119: 1977-1992.
546 31) Pierson, D. C., and G. A. Weyhenmeyer. 1994. "High resolution measurements of
547 sediment resuspension above an accumulation bottom in a stratified lake."
548 *Hydrobiologia* 284: 43-57. doi:10.1007/BF00005730.
549 32) Rojas, P., H. N. Ulloa, and Y. Niño. 2018. "Evolution and decay of gravity
550 wavefields in weak-rotating environments: a laboratory study." *Environmental*
551 *Fluid Mechanics* 18: 1509-1531. doi:10.1007/s10652-018-9609-5.
552 33) Rueda, F. J., S. G. Schladow, and S. O. Palmarsson. 2003. "Basin-scale internal
553 wave dynamics during a winter cooling period in a large lake." *Journal of*
554 *Geophysical Research* 108, C3, 3097. doi:10.1029/2001JC000942.
555 34) Schwab, D. J., and D. Beletsky. 1998. "Propagation of Kelvin waves along
556 irregular coastlines in finite-difference models." *Advances in water resources* 22:
557 239-245.
558 35) Shintani, T., A. Fuente, Y. Nino, and J. Imberger. 2010. "Generalizations of the
559 Wedderburn number: Parameterizing upwelling in stratified lakes." *Limnology and*

560 *Oceanography* 55: 1377-1389.
561 36) Simanjuntak, M. A., J. Imberger, and K. Nakayama. 2009. “Effect of stair-step and
562 piecewise linear topography on internal wave propagation in a geophysical flow
563 model.” *Journal of Geophysical Research* 114, C12020.
564 37) Steinman, B., W. Eckert, S. Kaganowsky, and T. Zohary. 1997. “Seiche-induced
565 resuspension in Lake Kinneret: A fluorescent tracer experiment.” *Water Air Soil*
566 *Pollution* 99: 123-131.
567 38) Steinmoeller, D. T., M. Stastna, and K. G. Lamb. 2019. “Calculating basin-scale
568 free oscillations in lakes on a rotating Earth.” *Ocean Modelling* 139, 101403: ISSN
569 1463-5003.
570 39) Stevens, C., and J. Imberger. 1996. “The initial response of a stratified lake to a
571 surface shear stress.” *Journal Fluid Mechanics* 312: 39-66.
572 doi: 10.1017/S0022112096001917.
573 40) Stocker, R., and J. Imberger. 2003. “Energy partitioning and horizontal dispersion
574 in a stratified rotating lake,” *Journal of Physical Oceanography* 33: 512-529.
575 41) Thompson, R. O. R. Y., and J. Imberger. 1980. “Response of a numerical model of
576 a stratified lake to wind stress.” *Proceedings of the International Symposium on*
577 *Stratified Flows* 2: 562-570.
578 42) Ulloa, H. N., A. Fuente, and Y. Niño. 2014. “An experimental study of the free
579 evolution of rotating, nonlinear internal gravity waves in a two-layer stratified
580 fluid.” *Journal Fluid Mechanic*s 742: 308-339. doi:10.1017/jfm.2014.10.
581 43) Ulloa, H. N., K. B. Winters, A. De la Fuente, and Y. Niño. 2015. “Degeneration of
582 internal Kelvin waves in a continuous two-layer stratification.” *Journal of Fluid*
583 *Mechanics* 777: 68-96.
584 44) Umlauf, L., and H. Burchard. 2003. “A generic length-scale equation for
585 geophysical turbulence models.” *Journal of Marine Research* 61: 235-265.
586 45) Vlasenko, V., and K. Hutter. 2002. “Numerical experiments on the breaking of
587 solitary internal waves over a slope-shelf topography.” *Journal of Physical*
588 *Oceanography* 32: 1779-1793.
589 46) Wake, G. W., G. N. Ivey, and J. Imberger. 2005. “The temporal evolution of
590 baroclinic basin-scale waves in a rotating circular basin.” *Journal Fluid Mechanics*
591 523: 367-392. doi:10.1017/S0022 11200 40023 44.
592 47) Wake, G. W., G. N. Ivey, J. Imberger, N. R. McDonald, and R. Stocker. 2004.
593 “Baroclinic geostrophic adjustment in a rotating circular basin.” *Journal Fluid*

Mechanics 515: 63-86. doi:10.1017/S0022 11200 40002 30.

48) Walters, R. A., E. Hanert, J. Pietrzak, and D. Y. Roux. 2009. "Comparison of unstructured, staggered grid methods for the shallow water equations." *Ocean Modelling* 28, Issues 1-3, 106-117: ISSN 1463-5003. doi:0.1016/j.ocemod.2008.12.004.

49) Warner, J. C., C. R. herwood, H. G. rango, and R. P. Signell. 2005. "Performance of four turbulence closure models implemented using a generic length scale method." *Ocean Modelling* 8: 81-113.

50) Wüest, A., and A. Lorke. 2003. "Small-scale hydrodynamics in lakes." *Annual Review of Fluid Mechanics* 35: 373-412.

51) Zhang, Y., and A. M. Baptista, 2008. "SELFE: A semi-implicit Eulerian-Lagrangian finite- element model for cross-scale ocean circulation." *Ocean Modelling* 21: 71-96. doi:10.1016/j.ocemod.2019.101403.

608 **List of tables**

612 **List of figures**

638

Figure 9 Internal waves in a circular basin using nesting grids. (a) Multigrid with the grid size of 100 m, 200 m and 400 m from the edge to center. (b) Density interface elevation $(x,\ y)$ = (10000 m, 15000 m). 100 m, 500 m and nesting grids.

Figure 10 (a) Conical basin. (b) Interface displacement of structured and unstructured grids.

Figure 11 Interface displacement for a conical basin. (a) Initial of structured grids. (b) Structured grids at 10 h. (c) Structured grids at 20 h. (d) Initial of unstructured grids. (e) Unstructured grids at 10 h. (f) Unstructured grids at 20 h.

651 Table 1 Conditions for surface and internal waves

Basin type	Wave type	Rossby radius (m)	Grid system	grid size (m)	Rossby-grid factor	Er (%)
Circular basin	Surface waves	2.71 x10^5	Structured	1000	270	2.1
				2500	108	6.5
				5000	54	8.5
			Unstructured	1780	152	0.7
	Internal waves	4540	Structured	100	45	7.5
				200	23	11.0
				500	9	12.8
				1000	5	16.6
			Unstructured	500	9	-
Conical basin	Internal waves	4540	Structured	500	9	5.7
			Unstructured	500	9	-

652 Note that Rossby radius for a conical basin is assumed to be the same as a circular basin.

653

654 Table 2 Normalized frequency of each mode for surface waves

mode	σ_k	A_k
1	6.9986	-0.4534
2	-7.38357	-0.3849
3	21.4002	-0.0349
4	-21.4730	-0.0379
5	34.2862	-0.0135
6	-34.3140	-0.0143
7	47.0196	-0.0072
8	-47.0343	-0.0075

655

656

657 Table 3 Normalized frequency of each mode for internal waves

mode	σ_k	A_k
1	0.5934	-0.6920
2	-1.4418	-0.1746
3	2.6072	-0.0197
4	-2.6696	-0.0408
5	4.0230	-0.0098
6	-4.0491	-0.0160
7	5.4475	-0.0058
8	-5.4617	-0.0083

658

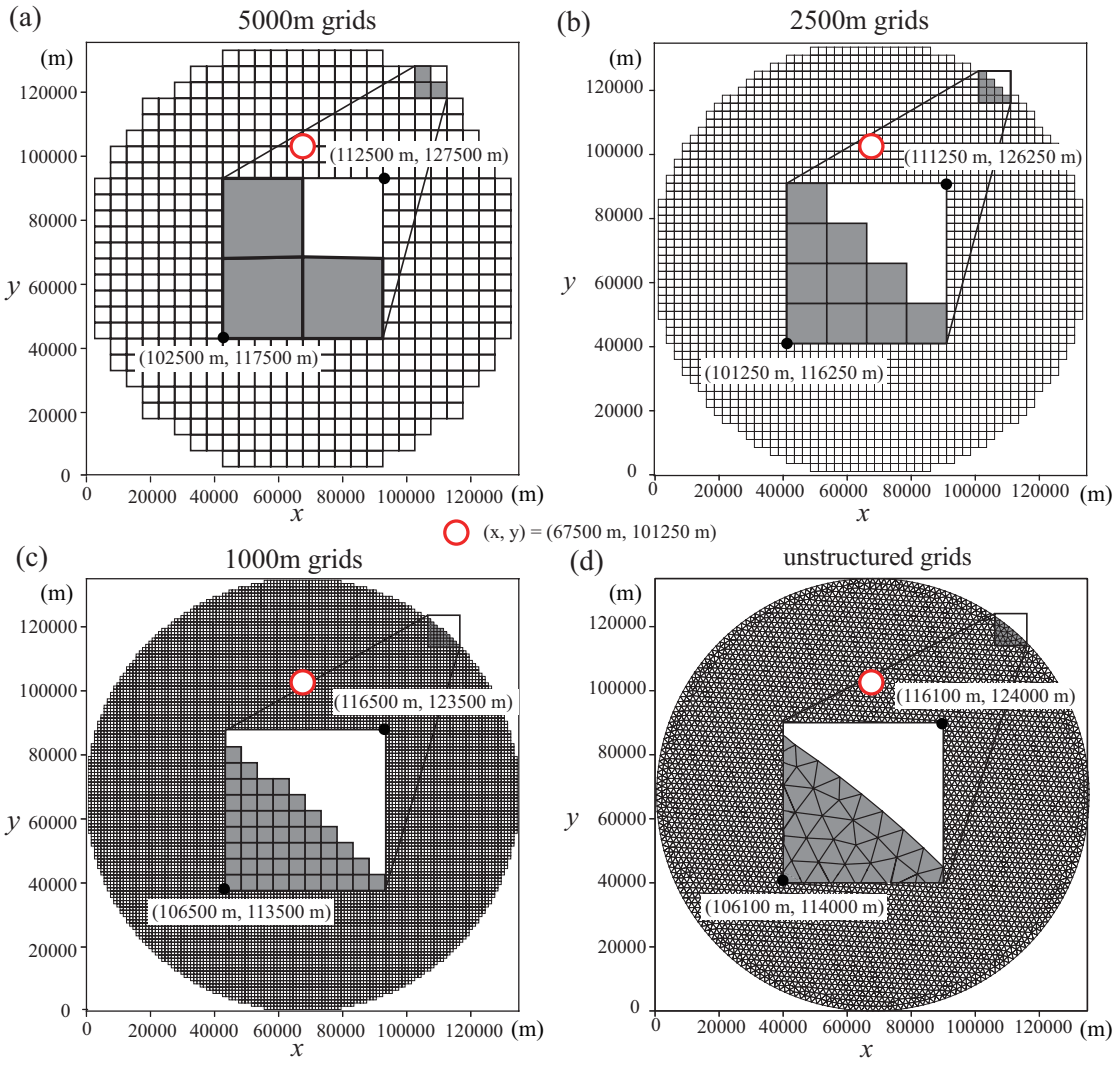

659

660 Figure 1 Surface waves in a circular basin. Structured grids with a grid size of (a)
661 5000 m, (b) 2500 m, and (c) 1000 m. (d) Unstructured grids with a representative
662 scale of 1780 m.

663

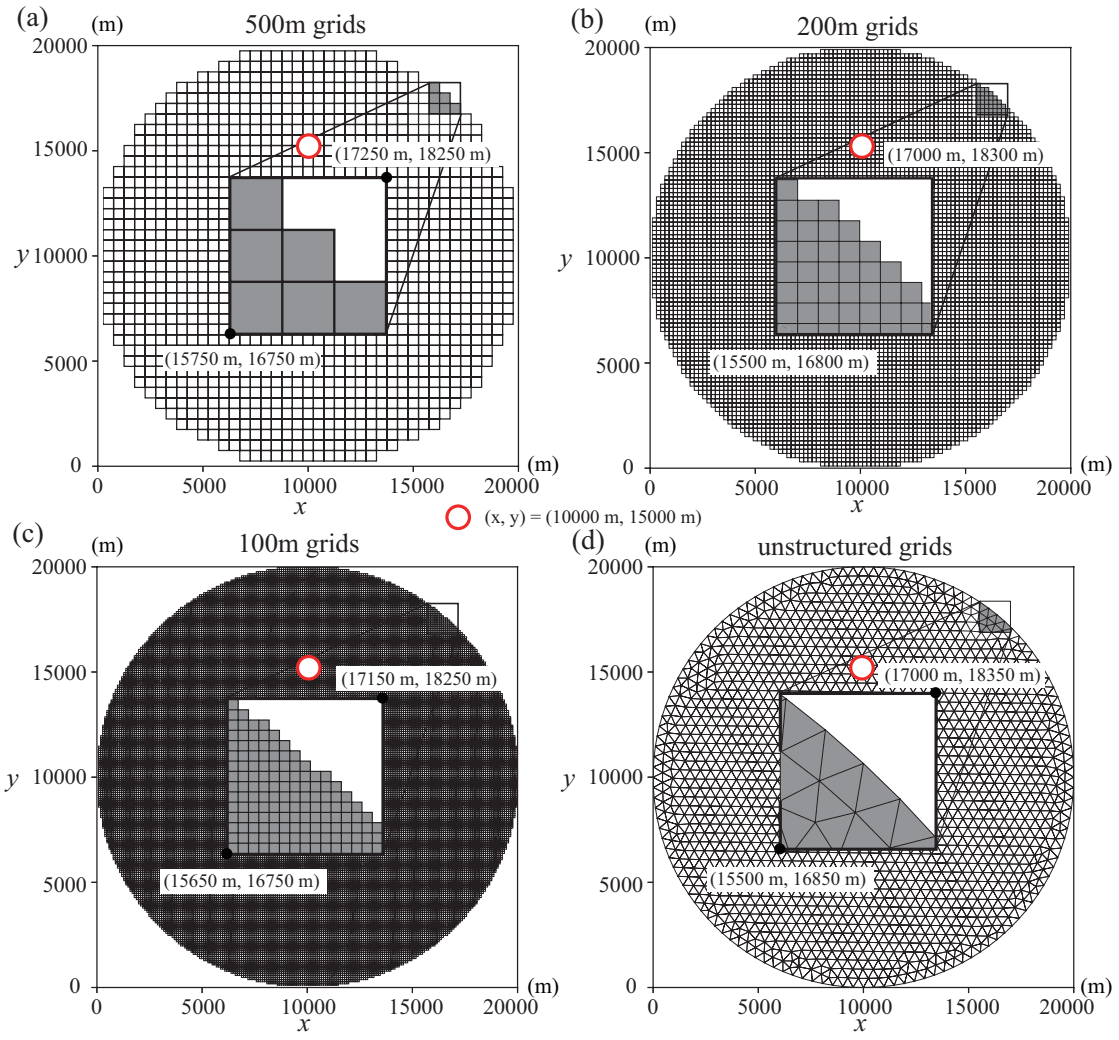

Figure 2 Internal waves in a circular basin. Structured grids with the grid size of (a) 500 m, (b) 200 m, and (c) 100 m. (d) Unstructured grids with a representative scale of 500 m.

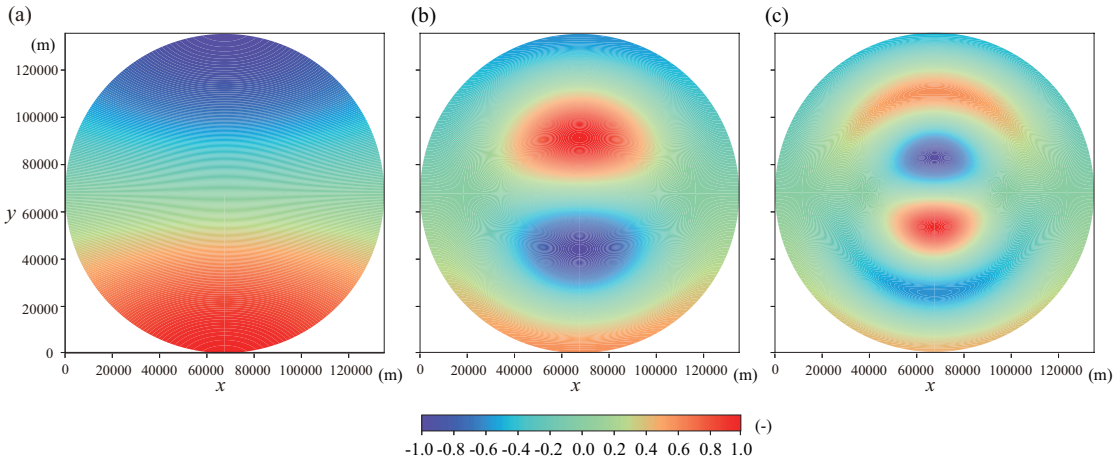

672

673 Figure 3 Water surface elevations. (a) SKW (mode 1). (b) SPW (mode 2). (c) SPW

674 (mode 3).

675

676

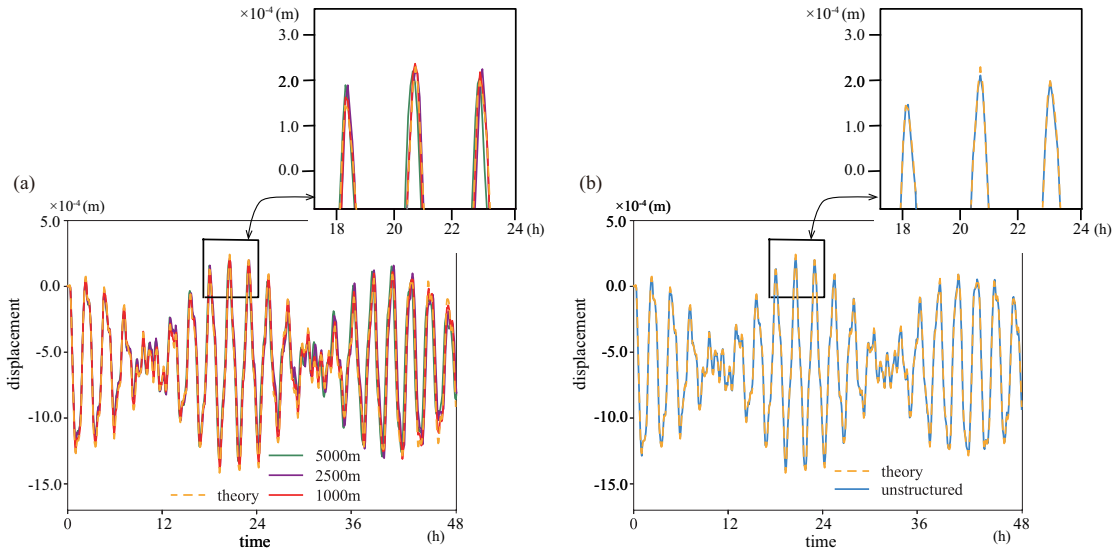

677

678 Figure 4 Water surface elevation (x, y) = (67500 m, 101250 m). (a) Structured grids

679 and theoretical solutions. (b) Unstructured grids and theoretical solutions.

680

681

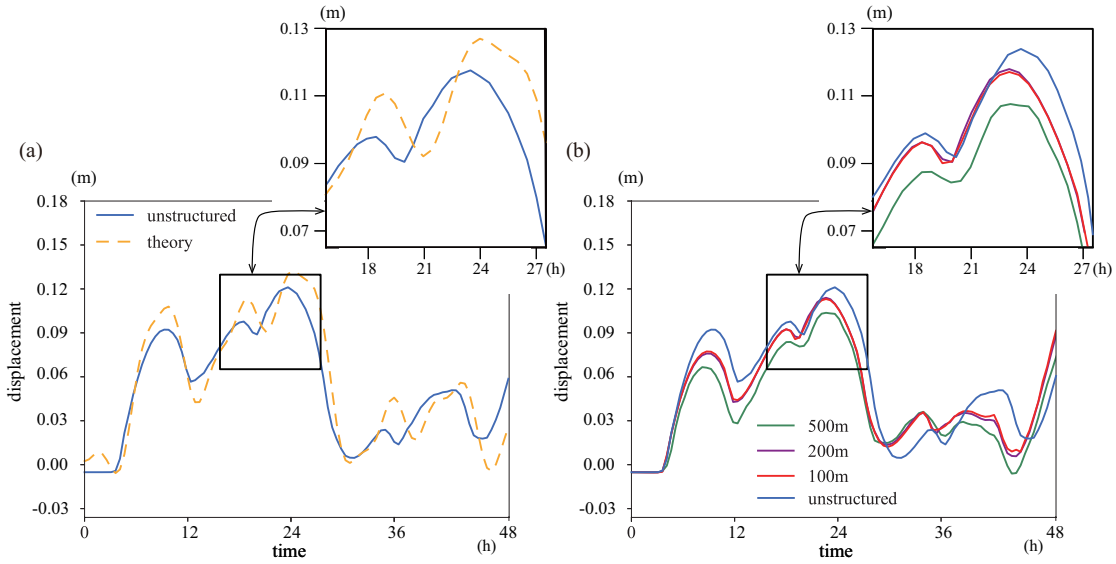

682

683 Figure 5 Density interface elevation (x, y) = (10000 m, 15000 m). (a) Unstructured

684 grids and theoretical solution. (b) Structured grids and unstructured grids.

685

686

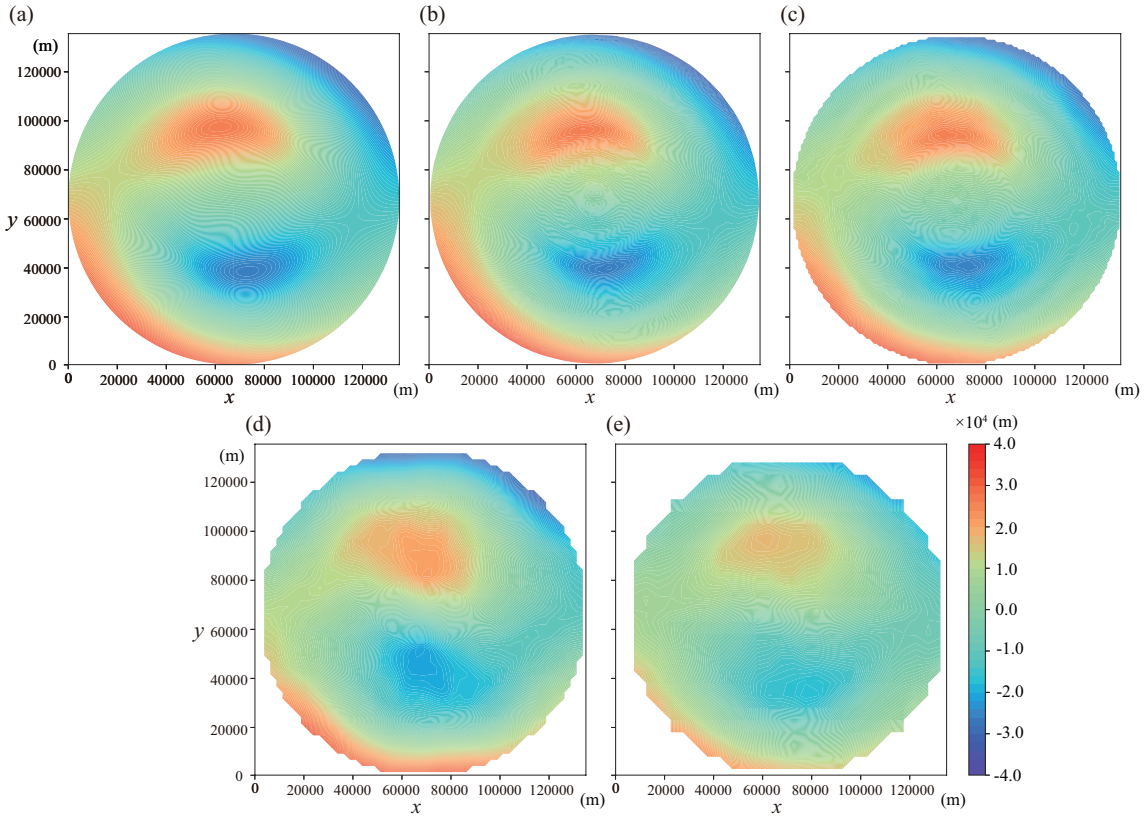

687

688 Figure 6 Water surface elevation at the energy time scale, T_E. (a) Theoretical

689 solution. (b) Unstructured grids. (c) 1000 m grids. (d) 2500 m grids. (e) 5000 m grids.

690

691

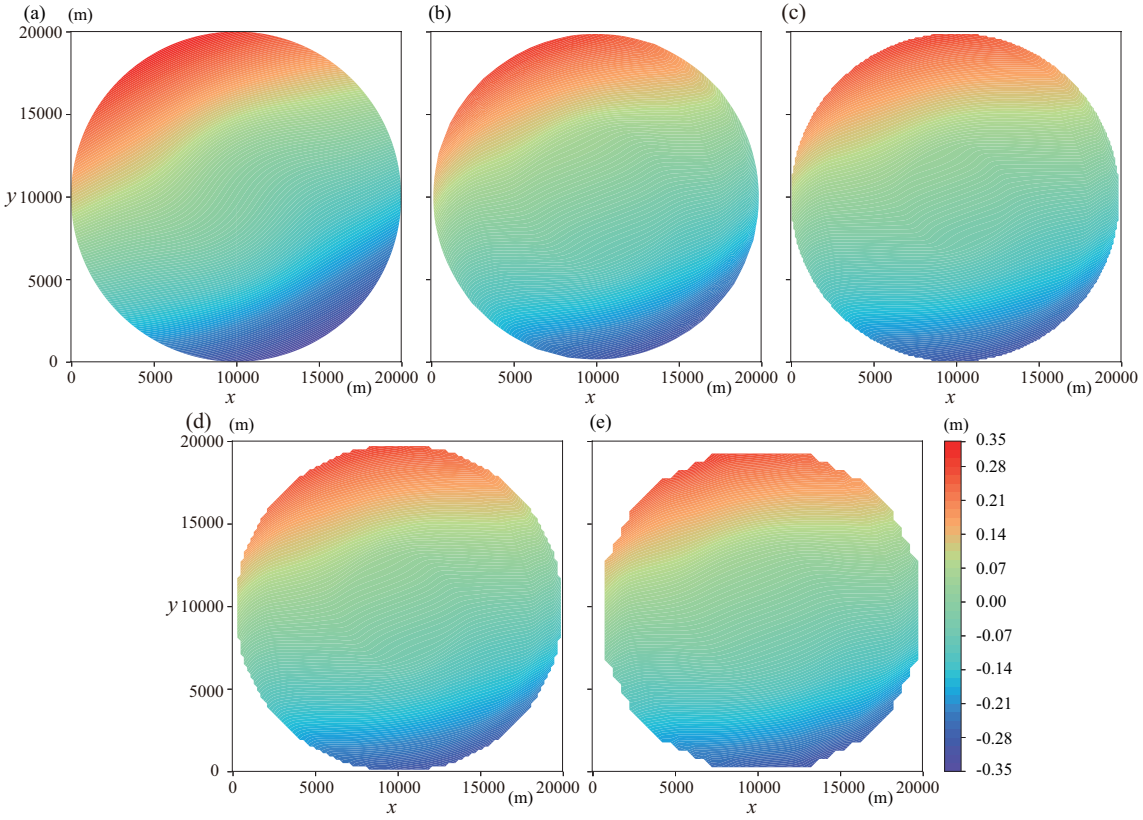

692

693 Figure 7 Internal wave elevations at the energy time scale, T_E. (a) Theoretical

694 solution. (b) Unstructured grids. (c) 100m grids. (d) 200m grids. (e) 500m grids.

695

696

697

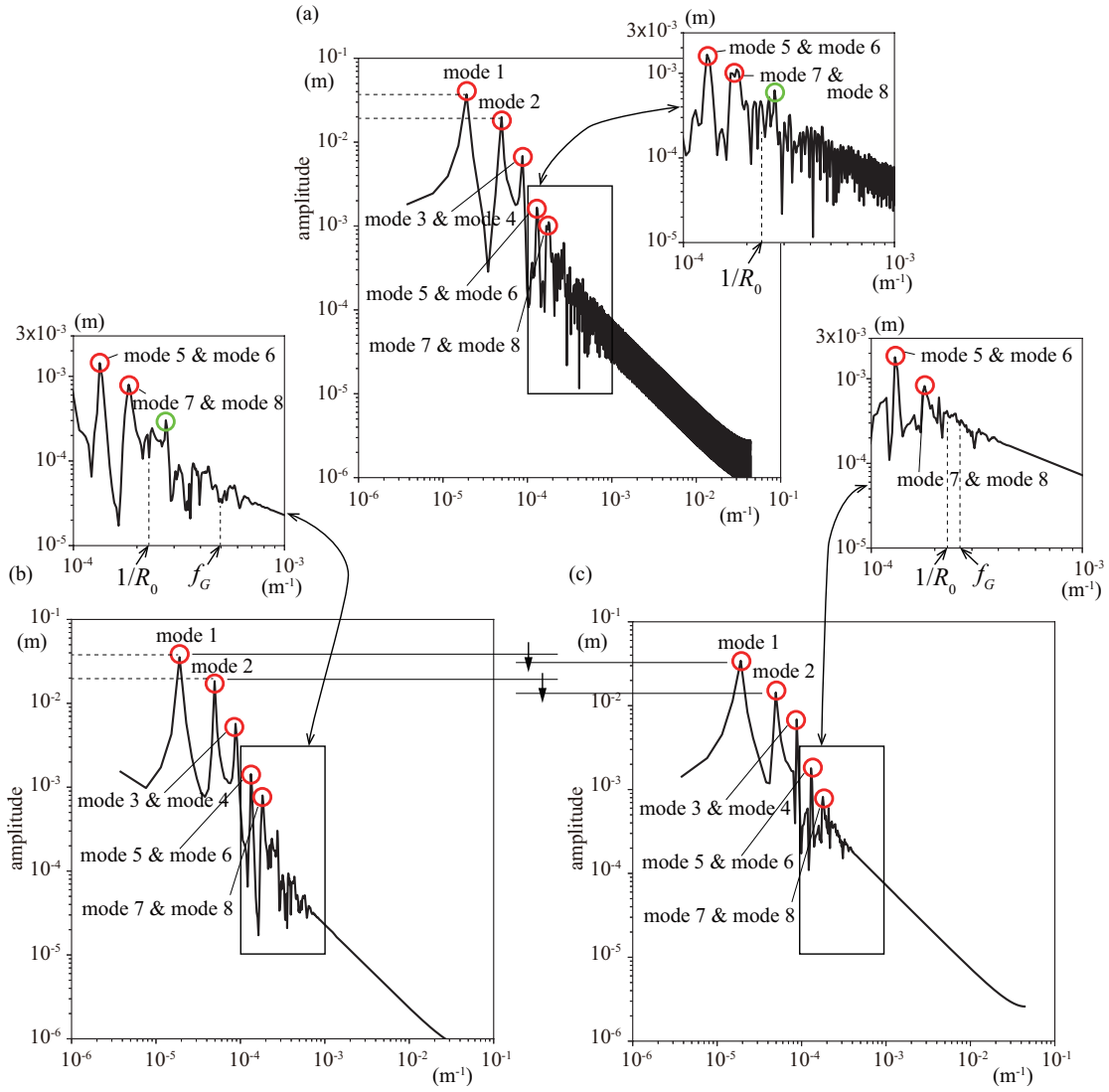

Figure 8 Spectrum of density interface elevation $(x,\ y)$ = (10000 m, 15000 m). (a) Unstructured grids. (b) 500 m grids. (c) 1000 m grids.

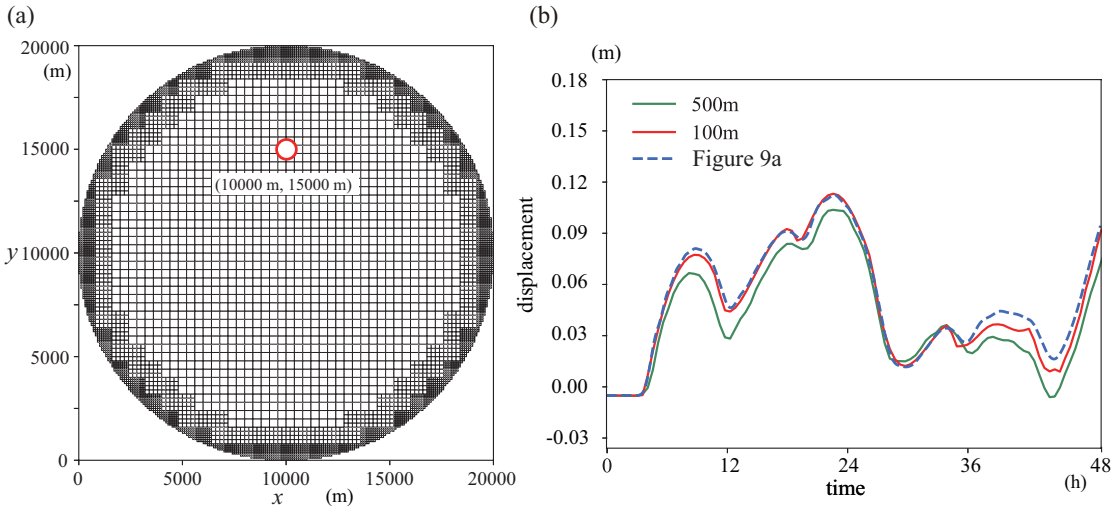

Figure 9 Internal waves in a circular basin using nesting grids. (a) Multigrid with the grid size of 100 m, 200 m and 400 m from the edge to center. (b) Density interface elevation $(x,\ y)$ = (10000 m, 15000 m). 100 m, 500 m and nesting grids.

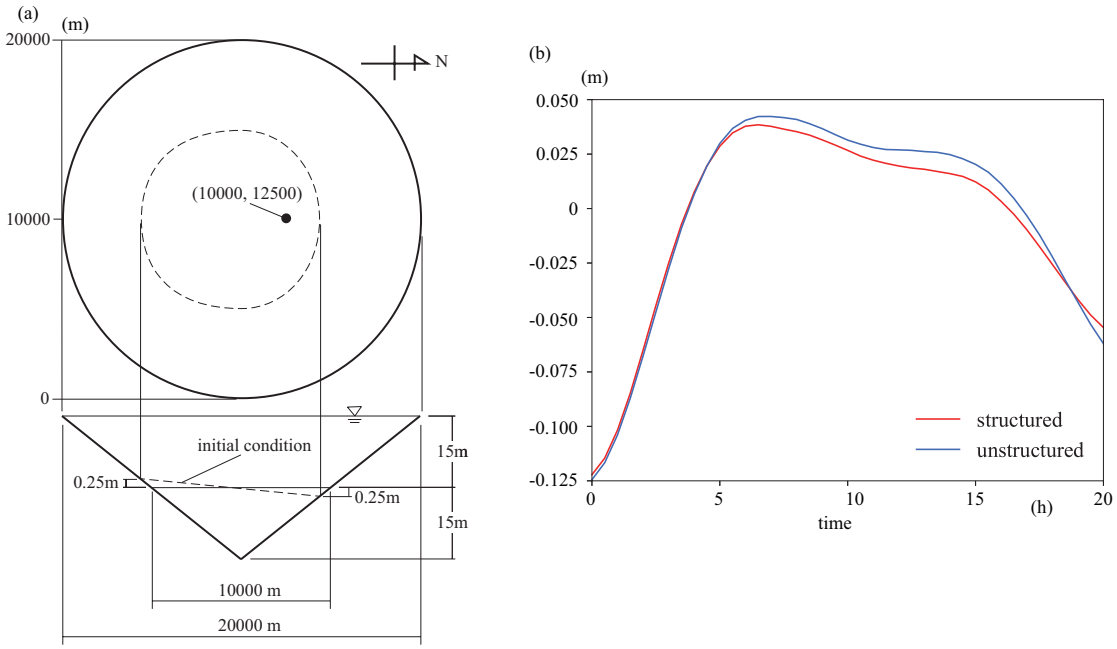

709

710 Figure 10 (a) Conical basin. (b) Interface displacement of structured and unstructured

711 grids.

712

713

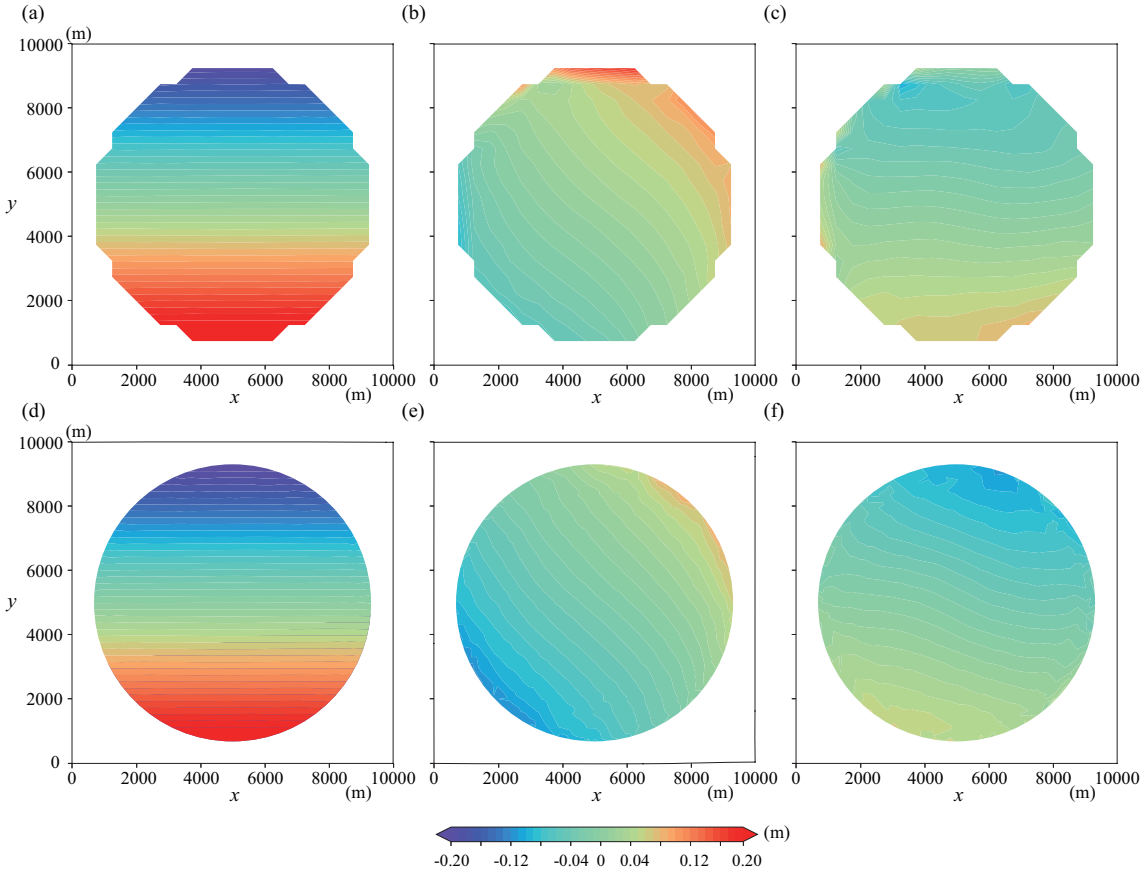

Figure 11 Interface displacement for a conical basin. (a) Initial of structured grids. (b) Structured grids at 10 h. (c) Structured grids at 20 h. (d) Initial of unstructured grids. (e) Unstructured grids at 10 h. (f) Unstructured grids at 20 h.